ACS OMEGA

http://pubs.acs.org/journal/acsodf

Article

Efficient Removal of Inorganic and Organic Pollutants over a $NiCo_2O_4$@MOF-801@MIL88A Photocatalyst: The Significance of Ternary Heterojunction Engineering

Mahnaz Bakhtian, Negin Khosroshahi, and Vahid Safarifard*

Cite This: *ACS Omega* 2022, 7, 42901−42915

Read Online

ACCESS | Metrics & More | Article Recommendations | Supporting Information

ABSTRACT: Energy problems are a substantial concern in a global society that can be solved by replacing with sustainable energies. In recent years, designing nanomaterials as photocatalysts that can produce chemical energy with the utilization of infinite visible light energy became a new solution for water treatment. In the present study, $NiCo_2O_4$@MOF-801 has been synthesized with multiple properties, and then, a novel three-layer $NiCo_2O_4$@MOF-801@MIL88A photocatalyst has been successfully synthesized to improve meropenem degradation and Cr(VI) reduction. The prepared photocatalyst was characterized by XRD, IR, XPS, TEM, SEM, TGA, BET, EIS, PL, and UV−vis. According to the structural and optical analysis performed, the interaction between the components formed a heterojunction structure that prevented the recombination of charge carriers and increased the photocatalytic performance. Photocatalytic simulation tests also proved the reduction of chromium and degradation of antibiotics to find the optimal heterogeneous performance. As a result, the $NiCo_2O_4$@MOF-801@MIL88A composite can completely reduce Cr(VI) in 45 min, which is strongly preferable to any pure component's performance. Overall, this work offers a low-cost but high-efficiency material that can remove organic and inorganic contaminants from water.

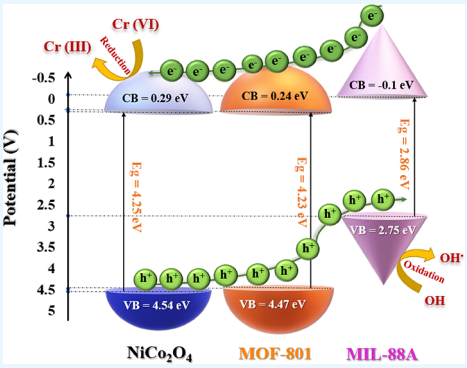

1. INTRODUCTION

Clean water has become more valuable as concerns about water crisis and drought spread due to global warming that will plague the entire world soon, and the conversion of solar energy into chemical energy to reduce environmental problems is a good alternative instead of traditional water treatment methods.[1,2] In the past few years, with the expansion of human societies, many organic and inorganic pollutants from factories and hospitals can leak through various routes into the water used in agriculture or drinking water.[3] Hexavalent chromium (Cr(VI)) is one of these toxic pollutants that enter the water systems from the wastes of plating, metallurgy, and other industries. According to the official organization of the World Health Organization (WHO), the permissible amount of chromium in drinking water is less than 0.05 micrograms per liter, and its higher concentration can be pathogenic and mutagenic.[4,5] Also, large quantities of antibiotics and analgesics enter the sewage due to improper disposal of hospital waste and excretion from the human body. Because of the prevalence of the Covid-19 pandemic and the increasing use of drugs such as painkillers and antibiotics, the concentration of these contaminants in the water is expected to increase significantly. These drugs are nondegradable and remain in the aqueous cycle.[6] Diverse methods are used to remove and destroy common water pollutants, including ultrafiltration, reverse osmosis, solvent extraction, adsorption, ion exchange, chemical deposition, and photocatalysis.[4,7] However, the main problem is that most of these methods can remove only one type of contaminant when there are usually a variety of contaminants in wastewater. Photocatalysis is one of the reliable methods to destroy or reduce pollutants, and in recent years, various materials have been used in this regard.[3,8−10] Substances that have photocatalytic properties absorb sunlight with a suitable bandgap, and separation of positive and negative charges occurs.[11] In aqueous medium, redox reactions can form active species of superoxide or hydroxide radicals, which also participate in subsequent reactions and can degrade or reduce certain substances.[6] For example, negative charges on the surface can reduce Cr(VI) to Cr(III).[11−13] Both the oxidation states mentioned are stable in water, but trivalent chromium is less dangerous and has less effect on DNA.[14,15] Generally, finding the right substance that has excellent photocatalytic activity to perform reactions in a short time is still debated.[16]

Metal−organic frameworks (MOFs) are porous crystalline structures made of metal nodes and linkers. There are more

Received: August 5, 2022
Accepted: November 2, 2022
Published: November 15, 2022

than 90,000 known MOFs, and this diversity has led to their widespread use in various applications.[5,17,18] Their main features include having a large specific surface area and controllable pore volume that make them suitable for catalytic activity.[19,20] Among them, MOF-801($Zr_6O_4(OH)_4$(fumarate)$_6\cdot xH_2O$) is considered in catalytic applications for its green and nontoxic synthesis methods as well as good water stability.[21] Also, iron-based MOFs such as MIL-88A,[22−24] MIL-88B,[25] MIL-100,[26] and MIL-101[27] were able to show good photocatalytic properties in absorbing visible light and removing contaminants. Between these iron-based MOFs, MIL-88A is not only easy to synthesize and environmentally friendly but also economically viable.[28] MIL-88A is a three-dimensional iron(III)-containing framework bonded by fumarate ions to create interconnected cages, which provide a large surface area with high porosity.[29] Recently, the design of MOF-on-MOF combinations has received a great deal of attention due to their unique features, such as the increased efficiency of the final composition relative to each pristine MOF.[30,31] The synthesis of one MOF in the presence of another MOF is an ideal strategy for fabricating heterogeneous catalysts to enhance structural properties. They make the structural and functional characteristics of the final product better than any of the MOFs alone.[13] Due to the narrow bandgap of MIL-88A and also the high porosity of MOF-801, combining them can have a positive synergistic effect to eliminate their shortcomings and improve their advantages.

Bimetallic oxides (AB_2O_4) are another structures that have recently received increased attention for their electronic and chemical properties and new applications.[32] Cobaltites with the general formula MCo_2O_4 (M = Zn Mn, Cu, Fe, Ni, or Mg) are one of these metal oxides that have a spinel structure. Nickel cobaltite is widely used due to its magnetic properties, narrow bandgap, and inexpensive precursors. Its main feature is the change of morphology along with the change of conditions and synthesis methods.[33,34] For cobaltite synthesis, many methods, such as hydrothermal/solvothermal, electrodeposition, electrospinning, template method, etc., have been reported. By changing the reaction conditions like solution pH, temperature, reaction time, type and amount of solvent, and the ratio of precursors, different morphologies and surfaces can be obtained.[35,36] Among all the available methods, hydro/solvothermal methods have advantages such as simplicity, uniformity, less polluting products, controllability, and low energy utilization.[35] Cobaltite nanostructures, with many catalytic sites, are widely used as catalysts or photocatalysts. However, there are still challenges like the relatively easy recombination of the electron−hole pairs, which is why the fabrication of multicomponent composites has been considered.

Herein, new nanocomposites are designed and synthesized from metal−organic frameworks and cobaltites. Initially, the $NiCo_2O_4$@MOF-801 core−shell nanocomposite was fabricated, which showed good photocatalytic performance in reducing Cr(VI) to Cr(III), but by adding MIL-88A as a third component to the previous composite, the reaction time was significantly reduced. Structural identification and property investigation of the synthesized nanocomposites were performed with different analyses such as XRD, DRS, SEM, TEM, TGA, PL, etc. and compared with each of the metal−organic frameworks before composition. Then, according to the new properties of the prepared nanocomposites, they were used for photocatalytic reduction applications of environmental pollutants such as hexavalent chromium or drugs. The project's main goal was the photocatalytic reduction of chromium, and then the degradation of various drugs was used to better prove the photocatalytic properties. It should be noted that finding the mechanism of the photocatalytic performance of the fabricated nanocomposite is also done using electrochemical measurements.

2. EXPERIMENTAL SECTION

2.1. Chemicals. All the reagents were of analytical grade and were used without further purification. Zirconium tetrachloride ($ZrCl_4$, 98%, Sigma-Aldrich), fumaric acid ($C_4H_4O_4$), formic acid (CH_2O_2), cobalt nitrate hexahydrate ($Co(NO_3)_2\cdot 6H_2O$), iron(III) chloride hexahydrate ($FeCl_3\cdot 6H_2O$, 98%), nickel nitrate hexahydrate ($Ni(NO_3)_2\cdot 6H_2O$), urea (CH_4N_2O), 2-methylimidazole ($C_4H_6N_2$), *N*,*N*-dimethylformamide (DMF, C_3H_7NO,99.5%), ethanol (C_2H_5OH, 99.7%), methanol (CH_3OH), acetone, and other necessary chemicals were procured from Merck company and used without further purification.

2.2. Preparation of Photocatalysts. *2.2.1. Synthesis of $NiCo_2O_4$.* For the synthesis of nickel cobaltite, the ZIF-67 precursor was first prepared. In this regard, 2-methylimidazole (3.3 g) and $Co(NO_3)_2\cdot 6H_2O$ (2.9 g) were dissolved in 20 mL of methanol. Then, the mixture was transferred into an autoclave and placed in an oven at 100 °C for 12 h. The obtained product was centrifuged and washed with methanol. The resulting powder was calcinated at 550 °C for 2 h. In the next step, 0.2 g of as-synthesized ZIF-67, 0.29 g of $Ni(NO_3)_2\cdot 6H_2O$, 0.58 g of $Co(NO_3)_2\cdot 6H_2O$, and 3.3 g of urea were dissolved in 35 mL of deionized water. Nickel cobaltite was prepared through the hydrothermal method at 12 h/120 °C. Thereafter, the as-synthesized powder was washed and collected by centrifugation using deionized water and ethanol several times. The black powder was washed with deionized water and ethanol and then dried at 60 °C overnight. Finally, the fabricated substance was calcinated at 2 h/350 °C.[37]

2.2.2. Synthesis of Zr-MOF-801. MOF-801 was synthesized according to the literature with slight modifications.[38,39] Fumaric acid (1.8 g) was added to the colorless solution that consists of $ZrCl_4$ (1.2 g) and water/formic acid (84 mL/18 mL) under continuous stirring, which resulted in a white solution. Finally, the mixture was stirred under reflux conditions at 120 °C. After 72 h, the resulting white powder was centrifuged and redispersed twice (1 h each time) in deionized water and ethanol with 50%−50% v/v%. Then, the procedure was repeated with acetone in the same way and dried at 65 °C to obtain the MOF-801 framework.

2.2.3. Synthesis of MIL-88(A). MIL-88(Fe) was prepared by following a previously reported literature work.[40] $FeCl_3\cdot 6H_2O$ (1.35 g) and fumaric acid (0.58 g) were dissolved in DMF:DI water (50%−50%) with continuous stirring. When the particles were dispersed as much as possible, the solution was put in a Teflon-lined autoclave and placed in an oven at 65 °C for 4 h. After completing the reaction, the orange powder was washed with deionized water and DMF and then dried similar to the abovementioned MOF.

2.2.4. Synthesis of $NiCo_2O_4$@MOF-801. For the synthesis of the $NiCo_2O_4$@MOF-801 composite, we poured MOF-801 precursors to nickel cobaltite. Fumaric acid (1.8 g) was added to the colorless solution that consists of $ZrCl_4$ (1.2 g) and water/formic acid (84 mL/18 mL) under continuous stirring, which resulted in a white solution. In a separate beaker, 0.2 g of

https://doi.org/10.1021/acsomega.2c05000
ACS Omega 2022, 7, 42901−42915

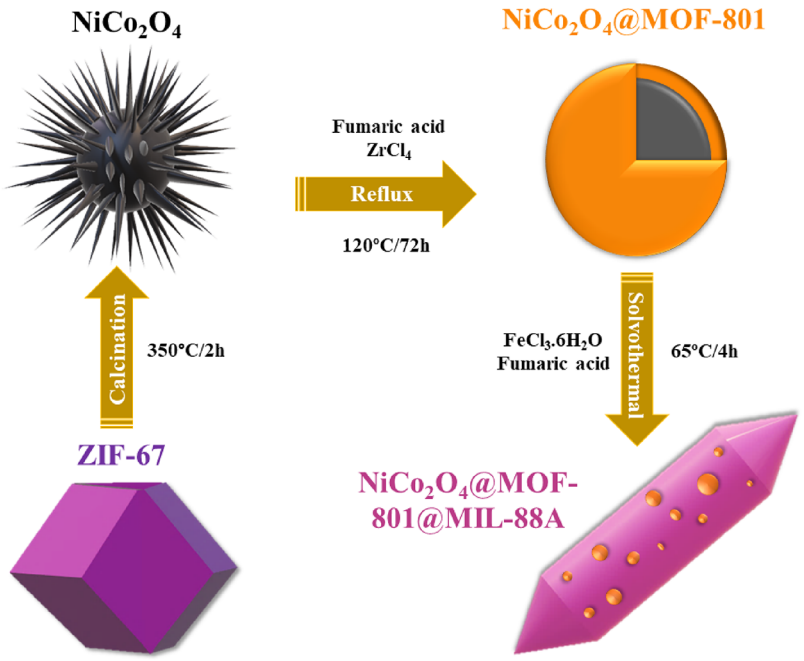

Figure 1. Synthesis process of $NiCo_2O_4$@MOF-801@MIL-88A heterojunctions.

nickel cobaltite was dispersed in water in an ultrasonic bath to be added to the previous solution. Finally, the mixture was stirred under reflux conditions at 120 °C. After 72 h, the resulting white solution was centrifuged and washed twice (1 h each time) with DI water and ethanol (50%−50%) and then dried at 80 °C to obtain the $NiCo_2O_4$@MOF-801 nanocomposite.

2.2.5. Synthesis of $NiCo_2O_4$@MOF-801@MIL-88(A). For the facile synthesis of the $NiCo_2O_4$@MOF-801@MIL-88A heterostructure, first, $FeCl_3{\cdot}6H_2O$ (1.35 g) and fumaric acid (0.58 g) were dissolved in DMF:DI water (50%−50%). Next, 0.3 g of $NiCo_2O_4$@MOF-801 was added to the above solution. After uniform dispersion of the particles, the solution was kept in an autoclave and was placed in an oven at 65 °C for 4 h. After completing the reaction, the as-synthesized heterostructure was washed with DI water and DMF several times and dried at 60 °C.

Figure 1 shows a summary of composite synthesis steps graphically.

2.3. Material Characterization. The infrared spectra were recorded on a Nicolet Fourier Transform IR, Nicolet 100 spectrometer in a 500−4000 cm^{-1} range using a KBr disk technique. X-ray powder diffraction (XRD) measurements were performed using a Philips X'pert diffractometer with monochromated Cu-Kα radiation (λ = 1.54056 Å). Mercury software prepared the simulated XRD powder pattern based on single-crystal data. X-ray photoelectron spectra (XPS) were recorded on a BESTEC (EA10) instrument, and the binding energy values were calibrated to the C (1s) peak. The sonicator used in this study was a Samkoon Sonicator with adjustable power output (maximum 400 W at 20 kHz). Elemental analysis of the nanocatalyst was provided by EDX analysis, measured by a TESCAN4992. The samples were characterized by a scanning electron microscope (SEM) (Philips XL 30 and S-4160) with gold coating. Transmission electron microscopy (TEM) images were provided using a Zeiss EM 900 electron microscope (Germany) operating at 80 kV. The surface area and pore size distribution were determined using a BET multilayer nitrogen adsorption method in a conventional volumetric technique with a Micromeritics ASAP 2020 instrument. UV−visible DRS spectra were obtained with a Shimadzu MPC-2200 spectrophotometer. A Netzsch Thermoanalyzer STA 504 was used for thermogravimetric analysis (TGA) with a heating rate of 10 °C/min under an air atmosphere. Fluorescence emission was performed by a Cary Eclipse MY13250011. The electrochemical measurements were carried out by a Metrohm Autolab PGSTAT204.

2.4. Photocatalytic Cr(VI) Reduction. In a typical reduction experiment, Cr(IV) solution (50 mL, 10 ppm) was prepared at first, and then a certain amount of $NiCo_2O_4$, MOF-801, MIL88A, $NiCo_2O_4$@MOF-801, or $NiCo_2O_4$@MOF-801@MIL88A and a known amount of oxalic acid as a hole scavenger at room temperature were added and were magnetically stirred in the darkness for 30 min to reach the adsorption−desorption equilibrium. After that, the sample was irradiated using a visible light lamp (500 W Xe lamp) until a color change was observed in the solution. After that, the solid photocatalyst was separated by centrifugation and the amount of chromium was measured with a UV−vis spectrophotometer at 350 nm. Solutions in different concentrations of chromium or different amounts of photocatalyst were tested. Also, to adjust the pH, different amounts of hydrochloric acid were added and the pH was checked simultaneously. Further, the photocatalytic efficiency was determined following the relation shown in eq 1:

$$(C_o - C_t)/C_o \times 100 \quad (1)$$

where C_o is the initial concentration of Cr(VI) species in mg L^{-1} and C_t is the concentration in mg L^{-1} at time t.

2.5. Photocatalytic Meropenem Degradation. For the degradation experiment, 10.0 mg of catalyst was dispersed into 50.0 mL of meropenem (40.0 mg/L) and stirred for 30 min in the dark. Then, a certain amount of H_2O_2 was put into the mixture solution as an oxidant, with visible light irradiation (500 W Xe lamp) simultaneously. At scheduled time intervals,

https://doi.org/10.1021/acsomega.2c05000
ACS Omega 2022, 7, 42901−42915

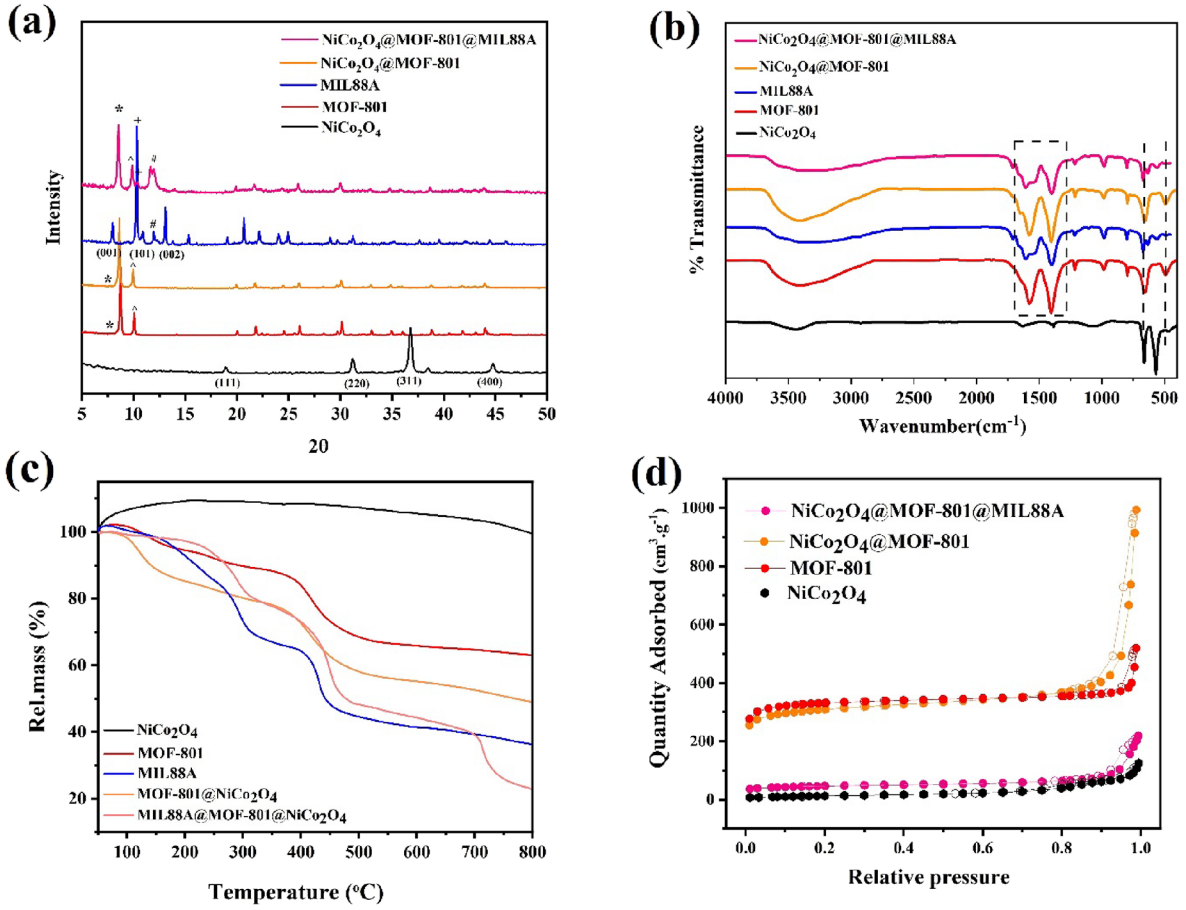

Figure 2. (a) Powder XRD pattern, (b) FT-IR spectra, (c) TGA plots, and (d) N_2 adsorption−desorption isotherms of $NiCo_2O_4$, MOF-801, MIL-88A, $NiCo_2O_4$@MOF-801, and $NiCo_2O_4$@MOF-801@MIL-88A.

2 mL of sample solution was taken from the reactor and separated by centrifugation. The concentration of the drug that remained in the solution was calibrated at its maximum absorption wavelength of 298 nm by using a UV−vis spectrophotometer. pH adjustment was performed using NaOH and HCl solutions, and the temperature was also maintained at 25 °C. Finally, by comparing the numbers obtained from the UV−vis spectrum and the above formula, the photocatalytic efficiency can be deduced.

2.6. Photoelectrochemical Measurements. Photoelectrochemical measurements were recorded in an electrochemical auto lab. In the three-electrode system, the counter electrode and a reference electrode were a Pt wire and an Ag/AgCl electrode (in saturated KCl), respectively. The working electrode was prepared as follows: The as-prepared materials (75%) were dispersed in a mixture solution containing NMP (*N*-methyl-2-pyrrolidone), PVDF (5%), and carbon black (20%) solution. Then, the resulting mixture was coated onto the Ni foam substrate and the foam was dried at 100 °C/12 h to remove the solvent. The photocurrent, electrochemical impedance spectra (EIS), and Mott−Schottky (MS) plots were measured in a Na_2SO_4 (0.2 M) aqueous solution as an electrolyte.

3. RESULTS AND DISCUSSION

3.1. Structure and Morphology. The powder XRD technique was employed to characterize the structural evolvement of the as-synthesized $NiCo_2O_4$, MOF-801, MIL-88A, $NiCo_2O_4$@MOF-801, and $NiCo_2O_4$@MOF-801@MIL88A. Figures S1−S3 compare the experimental PXRD patterns of pure materials and simulated patterns from single-crystal X-ray data, which confirms the eminent synthesis of MOF-801 and MIL-88A. As illustrated in Figure 2a, for $NiCo_2O_4$, its diffraction peaks at 18.9, 31.1, 36.7, and 44.6° can be assigned to the (111), (220), (311), and (400) reflections of face-centered cubic spinel $NiCo_2O_4$ (JCPDS no. 73-1702).[41] To characterize MOF-801, the major peaks are located near 8 and 10° followed by lower crystallinity signals that indicate proper structure synthesis.[42,43]

Incidentally, the PXRD pattern of the $NiCo_2O_4$@MOF-801 composite is also included in Figure 2a, which was more similar to that of MOF-801. The strong similarity of the $NiCo_2O_4$@MOF-801 pattern with the MOF-801 pattern supports the fact that the presence of nickel cobaltite does not affect the crystalline structure of the original MOF-801. This is due to the core−shell morphology of the $NiCo_2O_4$@MOF-801 composite and the presence of cobaltite nanoparticles in the shell of MOF-801, which prevent the direct X-ray diffraction from hitting the cobaltite nanoparticles, resulting in reduced intensity. Based on the results of PXRD and TEM analysis, the successful synthesis of the core−shell $NiCo_2O_4$@MOF-801 composite was confirmed. On the other hand, the strong (101) and (002) peaks' positions in the MIL-88A pattern approached 2θ = 10 and 13°, respectively.[23] Also, for the $NiCo_2O_4$@MOF-801@MIL-88A heterostructure, the

https://doi.org/10.1021/acsomega.2c05000
ACS Omega 2022, 7, 42901−42915

same result that MIL-88A has provided complete coverage on the previous structure can be drawn.

The crystallite diameter (D_c) of samples was obtained using the Debye−Scherrer equation (eq 2):[44]

$$D_c = K\lambda/\beta \cos\theta \quad (2)$$

where β is the breadth of the observed diffraction line at its half intensity maximum, K is the so-called shape factor, which adequately carries a value of about 0.9, and λ is the wavelength of the X-ray source used in XRD. The calculated crystalline domain sizes are 42, 100, 94.67, 100.7, and 80.4 nm for $NiCo_2O_4$, MOF-801, MIL-88A, $NiCo_2O_4$@MOF-801, and $NiCo_2O_4$@MOF-801@MIL88A, respectively.

FT-IR spectroscopy was employed for the identification of functional groups. As exhibited in Figure 2b, most peaks from 1400 to 1650 cm^{-1} in both MOF-801 and MIL-88A spectra belong to the symmetric and asymmetric vibration of −COOH groups in fumaric acid.[28,45] There is also a peak at 670 cm^{-1} related to the Fe−O bond in MIL-88A. For cobaltite nanoparticles, Co−O and Ni−O bonds have been identified at about 566 and 664 cm^{-1}, respectively.[46] According to the SEM and TEM images (Figure 2b), due to the core−shell structure of nanocomposites, their IR spectra are quite similar to the top layer, proving successful synthesis.

Thermogravimetric analysis was performed to recognize the possible thermal stability characteristics of MIL-88A(Fe) and Zr-MOF-801 compared with $NiCo_2O_4$@MOF-801 and $NiCo_2O_4$@MOF-801@MIL-88A. The results of TGA for the samples are illustrated in Figure 2c. Usually, the changes in the MOFs in the range of 100−200 °C are related to solvent evacuation. For both MOFs, the weight loss near 300 °C was attributed to the loss of solvent residues, and then at 500 °C, linkers (carboxylate groups) disintegrate.[42] As is evident, each step of the thermogram drop for the manufactured nanocomposites is related to the decomposition of one of the nanocomposite layers.

Tissue properties including the surface area along with pore orifice distribution are determinants of the adsorption capacity of the as-synthesized catalysts.[4] The porous properties of the as-synthesized samples are studied by N_2 adsorption−desorption isotherms. Figure 2d and Table 1 illustrate the adsorption−desorption isotherms, pore size distributions, and the full data. Figure 2d shows that the typical mesoporous structure of $NiCo_2O_4$, MOF-801, $NiCo_2O_4$@MOF-801, and $NiCo_2O_4$@MOF-801@MIL88A composites can be confirmed according to the type IV adsorption−desorption isotherm. Due to the low porosity and cavities of nickel cobaltite, the addition of secondary porous material such as MOF-801 can significantly affect the catalytic properties. The BET surface area of MOF-801 (1117 $m^2\ g^{-1}$) is much higher than that of pure $NiCo_2O_4$ (44 $m^2\ g^{-1}$), exhibiting that the $NiCo_2O_4$@MOF-801 heterostructure with a large surface area is conducive to providing the channels for charge transfer and generating the active sites. On the other hand, according to a previous report, MIL-88A has a very low specific surface area but can enhance the photocatalytic performance. As a result of MIL-88A addition to the $NiCo_2O_4$@MOF-801 heterostructure, the $NiCo_2O_4$@MOF-801@MIL88A surface area decreased to 161 $m^2\ g^{-1}$, which is still more porous than pure MIL-88A.[22]

Table 1. Physicochemical Parameters of the $NiCo_2O_4$, MOF-801, $NiCo_2O_4$@MOF-801, and $NiCo_2O_4$@MOF-801@MIL88A Photocatalysts

name of sample	BET surface area ($m^2\ g^{-1}$)	pore diameter (BJH) (Å)	total pore volume ($cm^3\ g^{-1}$)
$NiCo_2O_4$	44	107	0.127
Zr-MOF-801	1117	21	0.593
$NiCo_2O_4$@MOF-801	1074	39	1.03
$NiCo_2O_4$@MOF-801@MIL-88A	161	60	0.241

The morphology evolvement of $NiCo_2O_4$, $NiCo_2O_4$@MOF-801, and $NiCo_2O_4$@MOF-801@MIL88A was investigated by FESEM (Figure 3a−f). Also, the FESEM of the MOF-801 sample is presented in Figure S4. As illustrated in Figure 3a,b, MOF-derived $NiCo_2O_4$ nanoparticles have urchin-shaped morphology. Such a structure can enlarge the surface area to make more active sites participate in the redox reaction. Because of the decomposition of ZIF-67 blocks during the calcining process, the ZIF-67 polyhedra changed into flakes and sticks. Subsequently, the MOF-derived $NiCo_2O_4$ nanoparticles are used as the substrate for the growth of MOF-801 to form the $NiCo_2O_4$@MOF-801 heterostructure. The SEM image of $NiCo_2O_4$@MOF-801 depicted in Figure 3c,d reveals that the sample possesses a uniform spherical shape, and the average diameter is ∼128.48 nm. Also, the EDX of $NiCo_2O_4$@MOF-801 demonstrated in Figure S5 proves that the pure materials comprise only Zr and O. Based on mapping, not only MOF-801 elements were widely found on the composite surface but also small amounts of nickel and cobalt. From the SEM of images of $NiCo_2O_4$@MOF-801@ MIL-88A (Figure 3e,f), it can be observed that the nanocomposite maintains the needle-shaped microrods of MIL-88A(Fe) with an average size of 0.4−0.9 μm in length and 100−400 nm in diameter. Meanwhile, the existence of Fe, Zr, N, and O can be confirmed in Figure 3g. Figure 3h−k shows the elemental mapping analysis results, suggesting the homogeneous distribution of Fe, Zr, N, and O elements in the $NiCo_2O_4$@MOF-801@MIL-88A sample.

The surface morphologies of $NiCo_2O_4$@MOF-801 and $NiCo_2O_4$@MOF-801@MIL-88A have been carefully investigated by TEM. Figure 3l,m illustrates the TEM images of $NiCo_2O_4$@MOF-801, which proves the successful core−shell synthesis of Zr-MOF801 on nickel cobaltite nanoparticles. In the $NiCo_2O_4$@MOF-801 heterostructure, the polyhedra cobaltite is seen at the center of the spheres, with MOF-801 seen around it in a lighter color.

Furthermore, in Figure 3n,o, the placement of the $NiCo_2O_4$@MOF-801 spheres inside the MIL-88A needles can be observed, which confirms the double-shelled structure of this material. It can be deduced from the TEM images that MIL-88A is synthesized around $NiCo_2O_4$@MOF-801 via the self-assembly method (Figure 3n). The TEM image (Figure 3n) shows that $NiCo_2O_4$@MOF-801@ MIL-88A has a core−shell structure, which is consistent with the $NiCo_2O_4$@MOF-801 core (dark) and MIL-88A shell (light) structure. Also, the excess amount of $NiCo_2O_4$@MOF-801 is placed on the surface of MIL-88A. Of note, the images clearly illustrate how the nanospheres have closely adhered to the surface and inside of MIL-88A(Fe). Such contact is favorable to form enough interface to mediate charge transfer and enhance the synergetic effect of components during the photocatalytic process.

UV−vis diffuse reflectance spectroscopy was used to identify the optical properties and find the bandgap (E_g) value. As shown in figure 4a, the absorption edge is near 400 nm for

https://doi.org/10.1021/acsomega.2c05000
ACS Omega 2022, 7, 42901−42915

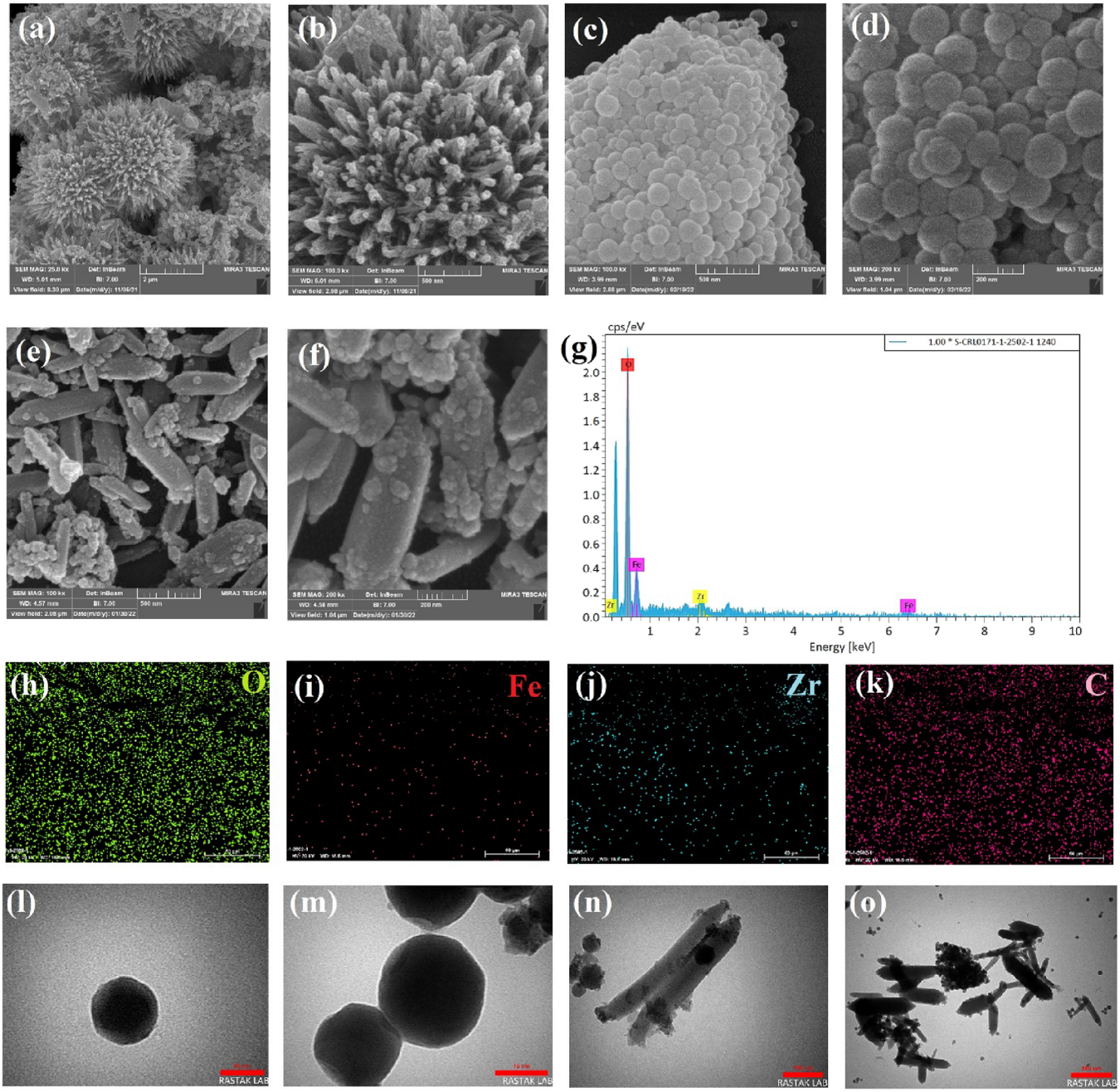

Figure 3. FE-SEM images of samples (a, b) $NiCo_2O_4$, (c, d) $NiCo_2O_4$@MOF-801, and (e, f) $NiCo_2O_4$@MOF-801, (g) EDX, (h–k) elemental mapping of $NiCo_2O_4$@MOF-801@MIL-88A, and TEM images of (l, m) $NiCo_2O_4$@MOF-801 and (n, o) $NiCo_2O_4$@MOF-801@MIL-88A.

nickel cobaltite and that close to 300 nm is related to MOF-801 and the $NiCo_2O_4$@MOF-801 composite. However, in the case of MIL-88A and $NiCo_2O_4$@MOF-801@MIL-88A, the absorption of visible light is well seen and they absorb light up to 650 nm. Using the Kubelka–Munk formula (eq 3) and plotting the Tauc graph $(\alpha h\nu)^2$ versus photon energy $(h\nu)$, the bandgap can be calculated[47]

$$(\alpha h\nu)^2 = c(h\nu - E_g) \tag{3}$$

where α, c, ν, and h stand for the absorbance, constant, frequency, and Planck constant, respectively. The bandgaps of $NiCo_2O_4$, MOF-801, and MIL-88A were evaluated to be 4.25, 4.23, and 2.86 eV, respectively, similar to those previously reported (Figure 4b). It was observed that with the addition of nickel cobaltite to MOF-801, the bandgap improved, but with the addition of MIL-88A, the bandgap was remarkably modified to 2.55 eV and the absorption of visible light increased.

Along with XRD and microscopy images, XPS analysis was used to prove the constituent elements and identify the final product structure.[48] Figure 4c illustrates the full-scan XPS spectrum showing that Fe, C, and O elements coexisted on the surface of $NiCo_2O_4$@MOF-801@MIL-88A(Fe). As shown in Figure 4d, the survey-scan XPS spectrum of Fe 2p could be split into Fe $2p^{1/2}$ (766.1 eV) and Fe $2p^{3/2}$ (744.3 eV), which proves the formation of the Fe–O bond of MIL-88A around the $NiCo_2O_4$@MOF-801 core–shell particles. In comparison with pure MIL-88A(Fe), the positive shift of Fe 2p peaks in

https://doi.org/10.1021/acsomega.2c05000
ACS Omega 2022, 7, 42901–42915

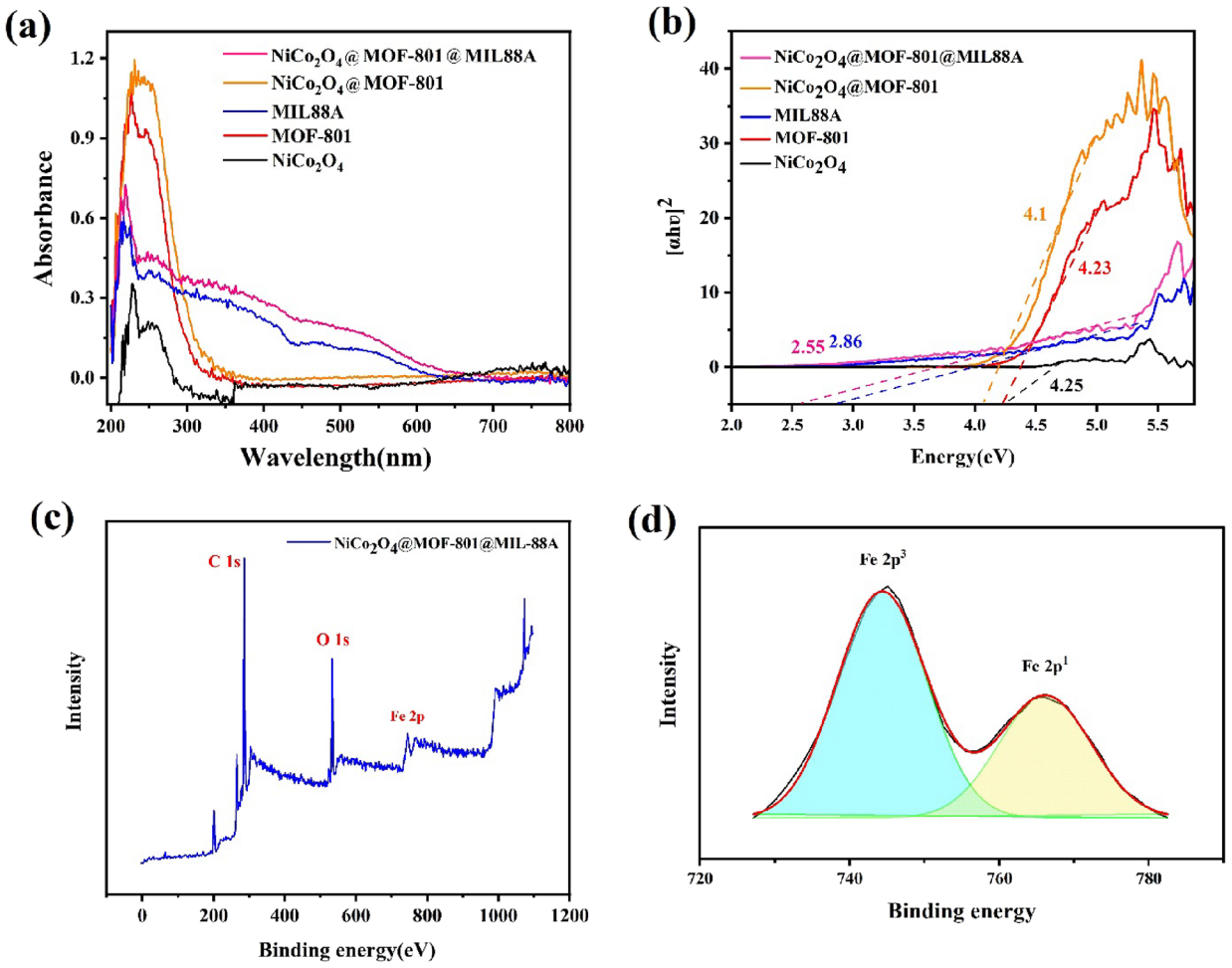

Figure 4. (a) UV−vis DRS spectra, (b) corresponding Tauc plots of $(\alpha h\nu)^2$ versus $h\nu$, (c) XPS spectra of $NiCo_2O_4$@MOF-801@MIL-88A, and (d) survey-scan Fe 2p.

the composite confirms a strong interaction and electron transfer between MIL-88A(Fe) and $NiCo_2O_4$@MOF-801.[49] Also, the characteristic peak of 285 eV derived from the XPS could be assigned to the carboxylate groups or C═C of fumaric acid and the sharp peak at a binding energy of 532 eV is related to the oxygen bonds of MIL-88A.[22]

3.2. Photocatalytic Activity. *3.2.1. Photocatalytic Activity of $NiCo_2O_4$@MOF-801@MIL88A for Cr(VI) Reduction.* The photocatalytic reduction of highly toxic heavy-metal Cr(VI) ions into nontoxic Cr(III) ions by using the $NiCo_2O_4$@MOF-801@MIL88A photocatalyst was also evaluated; the photoreduction activities of bare $NiCo_2O_4$, Zr-MOF-801 and $NiCo_2O_4$@MOF-801 were also investigated for comparison. Figure 5a shows the changes in the relative content of Cr(VI) in the reaction mixture over time, according to the composition of the composite, commencing with 30 min dark adsorption followed by 45 min photocatalysis. The UV−visible peaks observed at around 250 and 370 nm indicated the Cr(VI) peaks, and their intensity decreased with increasing the visible light illumination time, designating the reduction of Cr(VI) to Cr(III). In this work, a colorimetry method is utilized as evidence for the reduction of Cr(VI) to Cr(III). In this method, Cr(VI) was reacted with 1,5-diphenylcarbazide (DPC) dye, which, under acidic conditions, forms a purple-colored complex. As a result of a redox reaction, Cr(VI) is reduced to Cr(III), and DPC is oxidized to 1,5-diphenylcarbazone (DPCA). The Cr(VI) content in the supernatant was measured by using the standard DPC method. The colorless solution indicates the absence of Cr(VI) and the presence of Cr(III), which cannot form a complex with DPC.

The results illustrate that bare $NiCo_2O_4$ exhibits a pronounced removal performance for Cr(VI) ions, whereas almost no Cr(VI) photoreduction activity is observed for bare Zr-MOF-801. The $NiCo_2O_4$@MOF-801 heterostructure shows an enhanced photoreduction activity compared to the bare components, suggesting a synergistic effect between $NiCo_2O_4$ and Zr-MOF-801. With the addition of MIL88A into the previous binary structure, the Cr(VI) reduction of the $NiCo_2O_4$@MOF-801@MIL88A photocatalyst was slightly enhanced. As depicted in Figure 5a, the removal efficiency of the $NiCo_2O_4$@MOF-801@MIL88A ternary photocatalyst for Cr(VI) within 45 min increased to 100%, which is due to the increasing rate of electron−hole separation in the ternary composite.

The fundamental influence of catalyst's presence, visible light irradiation, pH effect, and hole scavenger on the photocatalytic Cr(VI) reduction has been examined in Figure 5b. The results show that the concentration of simulated chromium solution remains unchanged in the absence of each parameter. According to the reported results, in the dark time or the test without light, a small amount of the pollutant is absorbed by the catalyst. During light irradiation, Cr(VI) is

https://doi.org/10.1021/acsomega.2c05000
ACS Omega 2022, 7, 42901−42915

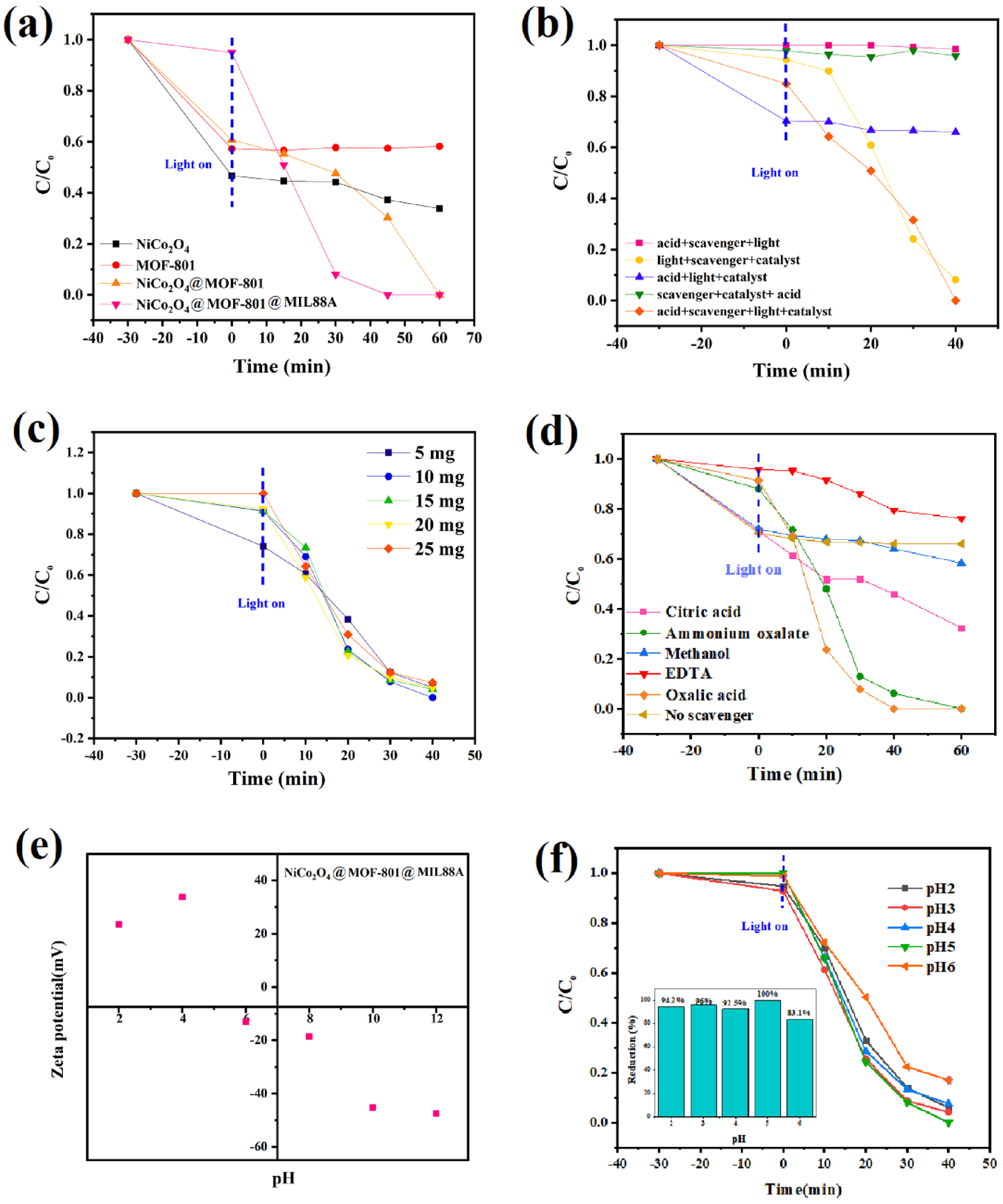

Figure 5. (a) Catalytic reduction of Cr(VI) to Cr(III) catalyzed by different catalyst types, (b) time-dependent plot for $NiCo_2O_4$@MOF-801@MIL-88A under various conditions, and effects of (c) catalyst dosage, (d) hole scavenger, (e) zeta potential of $NiCo_2O_4$@MOF-801@MIL-88A in different pH levels, and (f) pH adjustment.

removed from the reaction medium during the photocatalytic process. Also, in the test without a catalyst, there was no significant change in the amount of the catalyst. Considering that the chromium reduction reaction is carried out through electrons, the use of hole scavengers can greatly increase the charge separation and ultimately increase the photocatalytic

https://doi.org/10.1021/acsomega.2c05000
ACS Omega 2022, 7, 42901−42915

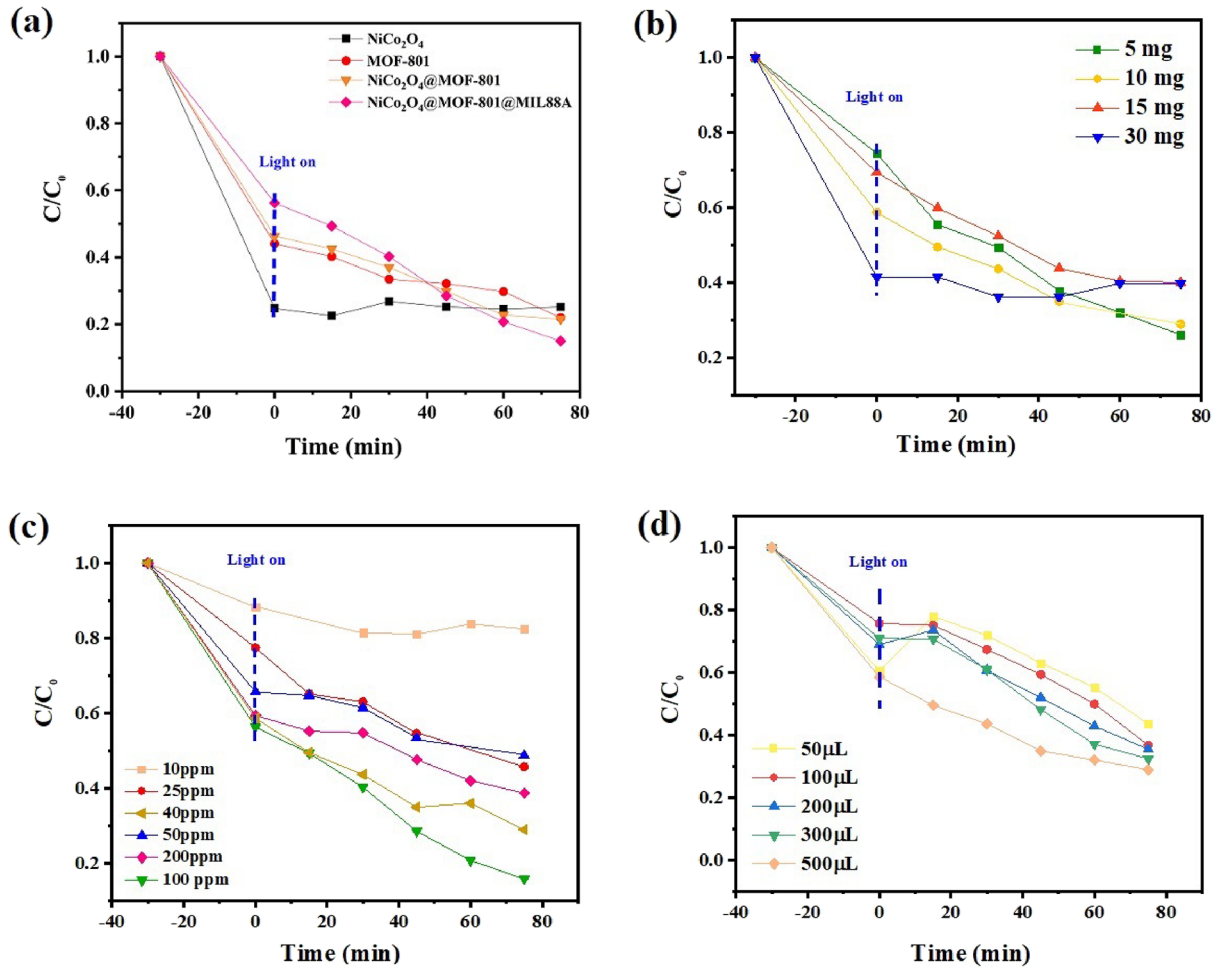

Figure 6. (a) Photocatalytic meropenem degradation dynamics plots and influences of (b) catalyst dosage, (c) initial drug concentration, and (d) H_2O_2 amount on the meropenem degradation performance over $NiCo_2O_4$@MOF-801@MIL-88A.

performance. In addition, the acidic conditions and existence of abundant H^+ facilitate the photocatalytic Cr(VI) reduction. It confirms the necessity of the presence of acid, catalyst, light, and hole scavenger to reach high photocatalytic performance.

In the following, the effects of different factors on the photocatalytic of Cr(VI) reduction over $NiCo_2O_4$@MOF-801@MIL88A were investigated, including the photocatalyst amount, various h^+ trappers, and pH effect. The effect of catalyst dose on the photocatalytic reduction of chromium was measured by varying catalyst amounts from 5 to 25 mg at fixed pH and Cr(VI) concentration. As illustrated in Figure 5c, the optimum catalyst dose was 10 mg according to photocatalytic results. The drop in the removal efficiency at a high catalyst loading can be attributed to the decreased diffusion of light and quenching of active sites.

Considering that the chromium reduction reaction is carried out through electrons, the use of hole scavengers can greatly increase the charge separation and ultimately increase the photocatalytic performance. The consumption of holes (h^+) will accelerate photo-induced electron−hole charge separation and will result in superior Cr(VI) reduction efficiency. Therefore, oxalic acid, EDTA, ammonium oxalate, citric acid, and methanol were utilized as scavengers to capture the photogenerated holes (Figure 5d). This result presents the reduction percentages of Cr(VI) for oxalic acid, ammonium oxalate, citric acid, methanol, and EDTA, which were found to be 100, 87, 48, 33, and 14.1, respectively, leading to the relative order in reduction efficiency as oxalic acid > ammonium oxalate > citric acid > methanol > EDTA. Particularly, due to the presence of two carboxyl groups in oxalic acid, it demonstrated a higher reactivity and better chromium reduction performance than the other hole scavengers.

As widely accepted, the pH value of the solution is an important factor in influencing the photocatalytic Cr(VI) reduction.[50] In this regard, zeta potential analysis was performed to measure the surface charge of the composite at different pH values. According to Figure 5e, in the acidic pH, the catalyst surface charge becomes more positive, which is effective in interacting and electrostatic repulsion with chromate anions. The zeta potential of $NiCo_2O_4$@MOF-801@MIL88A demonstrates the most positive charge at pH 4 (+33.8 mV), which indicates the strongest electrostatic interactions between the surface adsorbent and the anionic chromate solution.

Figure 5f illustrates the effect of pH on the Cr(VI) photoreduction over $NiCo_2O_4$@MOF-801@MIL88A in the pH range from 2 to 6. The composite material formed by electrostatic interaction had a better interface contact, which was more conducive to the separation of photogenerated carriers, thereby improving the photocatalytic performance. The iron-based MOF composites could catalyze the reaction in a wide pH range. By adjusting the electrical properties of the

https://doi.org/10.1021/acsomega.2c05000
ACS Omega 2022, 7, 42901−42915

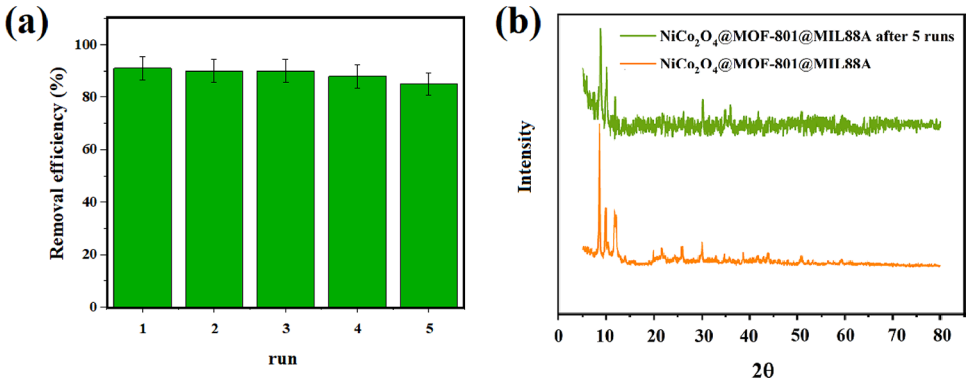

Figure 7. (a) Photostability tests over the $NiCo_2O_4$@MOF-801@MIL88A sample for the photodegradation of Cr(VI) and (b) XRD pattern of $NiCo_2O_4$@MOF-801@MIL88A after the photocatalytic reaction.

iron-based MOF catalytic surface, a composite material was formed by electrostatic interaction with substances with opposite charges. In this experiment, pH 5 was found to be an optimum pH and can reduce chromium 100% at 45 min. The existence of electrostatic repulsions between the $NiCo_2O_4$@MOF-801@MIL88A heterojunction and Cr(VI) inhibits the interaction with photogenerated electrons under alkaline conditions, so the Cr(VI) removal rate was reduced. As a result, the reduction percentage of Cr(VI) for pH 6 was 83.1%. In the as-synthesized ternary nanocomposite, MOFs provided enough surface area, active metal sites, and hydrophilic surface for efficient absorption and reduction. Under acidic conditions, $NiCo_2O_4$@MOF-801@MIL88A could effectively adsorb Cr(VI) through electrostatic attraction, and the adsorbed Cr(VI) ions were partly reduced to trivalent chromium Cr(III) (100%), resulting in the efficient adsorption and high removal of Cr(VI) from water. It should be mentioned that according to electrochemical measurements, $NiCo_2O_4$@MOF-801@MIL88A has a sufficient reducing power (0.29 eV) toward the reduction potential of hexavalent chromium, which is about 1.05 eV.

Subsequently, the synthesized catalyst was compared with the commercial P25 sample. P25, a commercially available TiO_2 consisting of 80% anatase and 20% rutile, as one of the oldest and widely used photocatalysts, is a good reference for comparison. In the photocatalytic reduction of hexavalent chromium, for a 40 mg L^{-1} solution with pH 2.5, P25 can remove 88% of chromium after 180 min.[51] However, the photocatalyst introduced in this article, $NiCo_2O_4$@MOF-801@MIL88A, can reduce more Cr(VI) in less time. So, $NiCo_2O_4$@MOF-801@MIL88A has a relatively higher photocatalytic activity than P25 for Cr(V) reduction.

The photocatalytic reaction follows a pseudo-first-order reaction ($-\ln(C_t/C_0) = K \times t$). The plot of $\ln(C_o/C)$ versus time presents a straight line, as shown in Figure S6, where the slope of which upon linear regression is equal to the apparent first-order rate constant K. The degradation rates obtained were 0.08, 0.014, and 0.007 min^{-1} for $NiCo_2O_4$@MOF-801@MIL88A, $NiCo_2O_4$@MOF-801, and $NiCo_2O_4$, which were consistent with the results obtained from the photoreduction tests. Since pure MOF-801 seems to not carry out the reaction, the rate constant is almost zero.

Finally, the leaching of the $NiCo_2O_4$@MOF-801@MIL88A photocatalyst was tested to investigate its stability and secondary pollution. This was performed by stopping the reduction reaction after 15 min by separating the catalyst from the reaction medium via filtration. The filtrate was used again, and the whole reaction was continued for another 45 min. According to Figure S7, no further reduction of Cr(VI) was observed, which confirmed the absence of active metals in the filtrate.

3.2.2. Photocatalytic Activity of $NiCo_2O_4$@MOF-801@MIL88A for Meropenem Degradation. The photocatalytic degradation of antibiotics such as meropenem, ceftriaxone, and ceftazidime (100 ppm) was carried out to investigate the influence of electron transfer on the catalyst performance. It should be noted that in the general comparison of the degradation of antibiotics, the degradation of meropenem demonstrates the best performance in 60 min (Figure S8). To achieve the adsorption−desorption equilibrium, meropenem and the catalyst were mixed in a dark condition for 30 min before the beginning of the photocatalytic reaction. As illustrated in Figure 6a, the pristine MOF-801 and $NiCo_2O_4$ exhibit poor photocatalytic performance, whereas the photocatalytic activity of the $NiCo_2O_4$@MOF-801@MIL88A heterojunction was enhanced obviously. The degradation efficiency of meropenem was calculated at 85% within 75 min for the $NiCo_2O_4$@MOF-801@MIL88A ternary composite. The results suggested that $NiCo_2O_4$, MOF-801, and MIL-88A were capable to promote the photocatalytic performance by a ternary heterojunction.

As shown in Figure 6b, the photocatalyst dosage effect on meropenem removal efficiency was explored. The antibiotic degradation efficiency within 75 min was found to be 91% for a 5 mg $NiCo_2O_4$@MOF-801@MIL88A dosage. However, increasing the amount of $NiCo_2O_4$@MOF-801@MIL88A to 30 mg only contributes to a faint increase in activity. Hence, 5 mg of $NiCo_2O_4$@MOF-801@MIL88A is the proper dosage for meropenem degradation.

Figure 6c illustrates the impact of initial meropenem concentration from 10 to 200 ppm on the photocatalytic ability of $NiCo_2O_4$@MOF-801@MIL88A under visible light. According to the results, the optimum initial antibiotic concentration was found at 100 ppm for efficient photodegradation. At lower concentrations, the frequency of collisions between the meropenem molecules and the catalyst surface was low, leading to the ineffectiveness of the degradation. The increase in the meropenem concentration from 100 to 200 ppm decreased the degradation performance due to the prevention of light transmission caused by meropenem molecules.

https://doi.org/10.1021/acsomega.2c05000
ACS Omega 2022, 7, 42901−42915

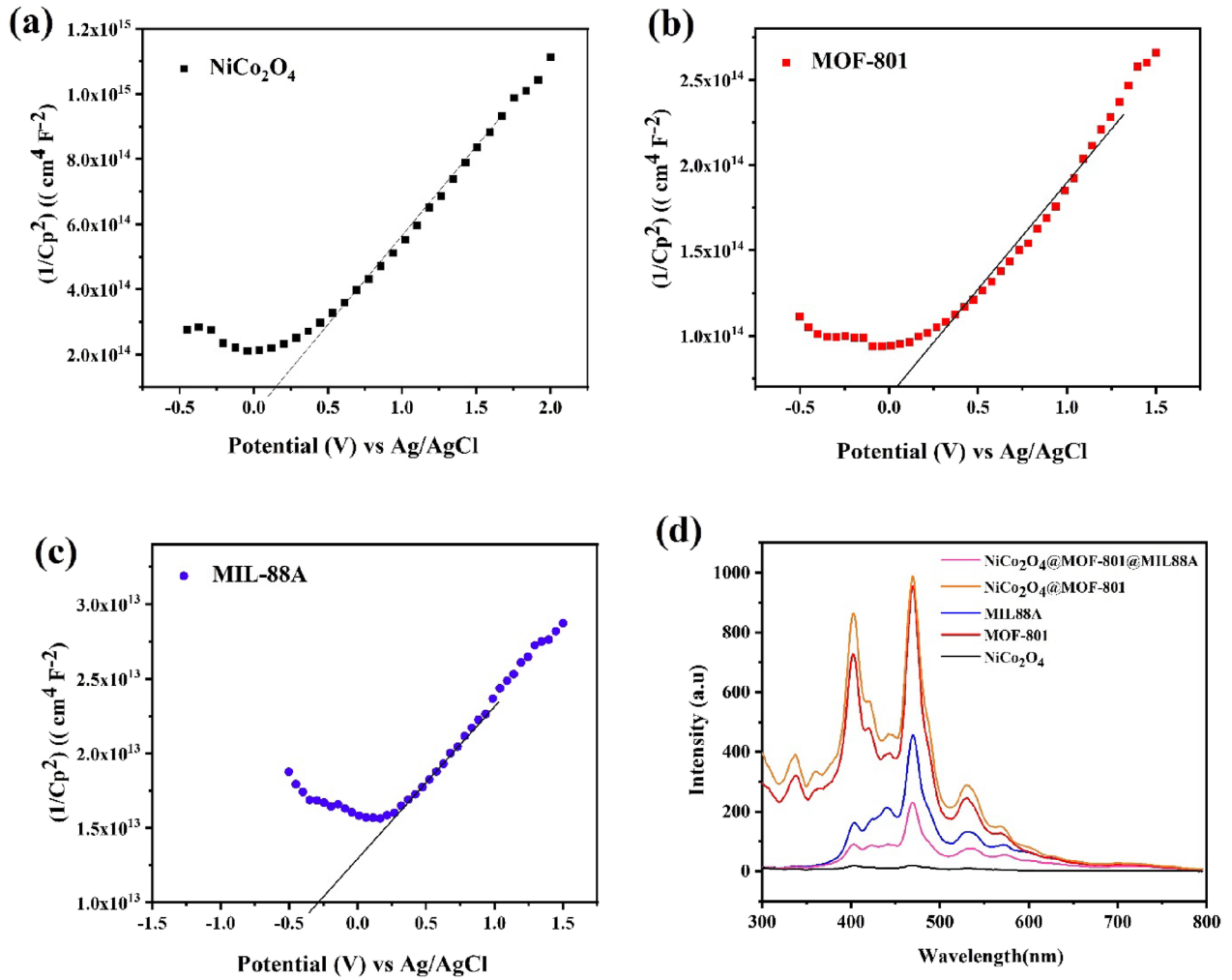

Figure 8. Mott−Schottky plots of (a) $NiCo_2O_4$, (b) MOF-801, and (c) MIL-88A. (d) PL spectra of the $NiCo_2O_4$@MOF-801@MIL-88A composite.

To further increase the photocatalytic activity of the catalyst, H_2O_2 was added as an oxidant to the solution. H_2O_2 acts as a photo-electron trapping agent and reduces the recombination of electron−hole pairs. The cleavage of H_2O_2 generated the reactive hydroxyl radicals ($OH^•$) for the degradation. The meropenem degradation percentage in the presence of H_2O_2 was calculated at 91%, while in the absence of oxidant, the antibiotic degradation efficiency of the $NiCo_2O_4$@MOF-801@MIL88A decreased to 60% (Figure 6d). The drug degradation reaction was also investigated in terms of kinetics. However, there is not a huge difference, but the slope of the three-layer composite graph was 0.01, which is higher than the rest of the materials and is in accordance with the photocatalytic tests performed (Figure S9).

To be an effective catalyst in practical applications, the reusability of the catalyst is a critical factor. The reusability of the photocatalyst was investigated for five consecutive cycles for each reaction separately. In each period, the catalyst was separated from the medium by centrifugation, and a sufficient amount of it was used for the next reaction. The results indicate no substantial loss of catalytic activity, demonstrating the excellent stability of the developed heterojunction during visible light irradiation (Figure 7a). Also, XRD analyses were performed on the used catalyst after five runs to prove that the structure was not destroyed (Figure 7b).

3.3. Mechanism for Improved Photocatalytic Activity over $NiCo_2O_4$@MOF-801@MIL-88(A). To understand the significantly improved performance of the $NiCo_2O_4$@MOF-801@MIL88A ternary heterojunction on chromium reduction and meropenem degradation, a series of optical and electrochemical measurements were carried out. The measurement of the energy band structure of $NiCo_2O_4$@MOF-801@MIL88A is helpful to determine the carrier transfer mechanism of ternary composite materials. The Mott−Schottky test was carried out to measure samples' flat band (E_{fb}) potentials using the Ag/AgCl electrode as reference electrodes. Figure 8a−c demonstrates the Mott−Schottky plots of $NiCo_2O_4$, MOF-801, and MIL-88A, respectively, which reveal the typical n-type semiconductivity (positive slope) for these samples. The E_{fb} values are 0.1, 0.05, and −0.3 eV (vs Ag/AgCl) for $NiCo_2O_4$, MOF-801, and MIL-88A, respectively. The E_{fb} potential is the same as the conduction band position (CB). Therefore, the E_{CB} values deduced are 0.297, 0.247, and −0.1024 eV vs NHE, respectively. Through analyzing the UV−vis diffuse reflectance spectrum to obtain the bandgap data of the sample (Figure 4b), it can be concluded that the valence band potentials (E_{VB}) are 4.547, 4.477, and 2.757 eV for $NiCo_2O_4$, MOF-801, and MIL-88A electrodes, respectively.

To figure out the factors related to the higher photocatalytic activity of $NiCo_2O_4$@MOF-801@MIL-88A composites, the

https://doi.org/10.1021/acsomega.2c05000
ACS Omega 2022, 7, 42901−42915

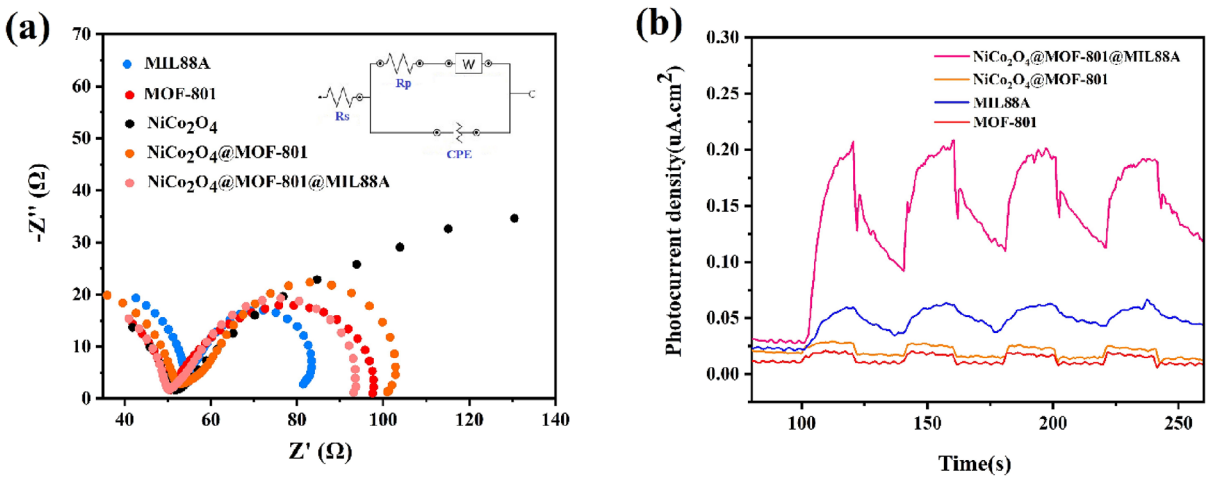

Figure 9. (a) EIS Nyquist impedance plots and (b) photocurrent plot of the $NiCo_2O_4$@MOF-801@MIL-88A composite.

photoluminescence spectra of as-prepared samples were measured. PL spectroscopy is a method to identify structures' optical and photochemical properties, and their signal strength is an effective criterion for reflecting the combination condition of charge carriers.[8] As shown in Figure 8d, the PL spectra of the prepared samples exhibited emission peaks centered at about 469 nm, and $NiCo_2O_4$@MOF-801@MIL-88A displays a lower PL intensity peak than the other samples, which means that the recombination rate of photoinduced carriers decreases. It indicates that the $NiCo_2O_4$@MOF-801@MIL-88A heterojunction has a strong ability to separate electron−hole pairs and improves the transfer efficiency of photogenerated carriers. It can also be pointed out that in the $NiCo_2O_4$'s PL, weak diffusion peaks can be attributed to the excitatory PL and are due to surface oxygen voids and defects in $NiCo_2O_4$ nanoparticles.[52,53] The pores within MOFs can also be utilized to encapsulate a large number of guest species as photonic units. The vast combination of possibilities enhanced the synergistic effects and enabled them to be a promising platform for realizing novel photocatalytic applications.

Electrochemical impedance spectroscopy (EIS) measurements were carried out to study the electrochemical behavior and charge transfer properties of the $NiCo_2O_4$@MOF-801@MIL88A and $NiCo_2O_4$@MOF-801 electrodes compared with their components.[54,55] Figure 9a shows the arc area of EIS Nyquist plots where the small circle radius indicates less resistance to separation of charge carriers. As can be seen, the $NiCo_2O_4$@MOF-801@MIL88A composite shows a smaller radius of semicircle arc than $NiCo_2O_4$@MOF-801, which implies that the electron transfer resistance of the composite decreased after the coupling of MIL88A. On the other hand, although the $NiCo_2O_4$@MOF-801 composite performed weaker than MOF-801, the pristine nickel cobaltite impedance improved significantly with compositing.

The separation of photogenerated charges over $NiCo_2O_4$@MOF-801@MIL-88A composites was investigated by photocurrent responses.[3,9] Electricity generation is a function that can prove the photoinduced charge transfer between components.[15] The transient photocurrent response experiment (Figure 9b) conducted at the same time indicated that $NiCo_2O_4$@MOF-801@MIL-88A had good photoresponse ability during the four on−off cycles of irradiation. $NiCo_2O_4$@MOF-801@MIL-88A exhibited a current density approximately 10 times higher than MOF-801@MIL-88A, which further indicated that the synthesized three-layer composite could effectively inhibit the recombination of photoinduced charge carriers.

According to EIS, PL, and photocurrent results, $NiCo_2O_4$@MOF-801 is not an effective photocatalyst. But, the addition of MIL-88A as the third layer enhances the electron transfer and reduces the recombination. As a result of the construction of $NiCo_2O_4$@MOF-801@MIL-88A, the photocatalytic activity of the ternary composite improved.

Based on the above experiments, an assumed photocatalytic mechanism for the $NiCo_2O_4$@MOF-801@MIL-88A composite is provisionally presented in Figure 10. To produce e^- and h^+, the $NiCo_2O_4$, MOF-801, and MIL-88A samples were stimulated by visible light irradiation. The photo-induced electrons can migrate from the MIL-88A's LUMO to the $NiCo_2O_4$'s conduction band (CB), which can accelerate the separation of photogenerated electrons−holes and lead to an increase in free electrons accumulated over the $NiCo_2O_4$'s conduction band. The $NiCo_2O_4$'s LUMO is more negative than the chromium standard redox potential (Cr^{6+}/Cr^{3+} = 1.05 eV). So, $NiCo_2O_4$@MOF-801@MIL-88A exhibited enhanced Cr(VI) reduction efficiency exposed to white light irradiation.

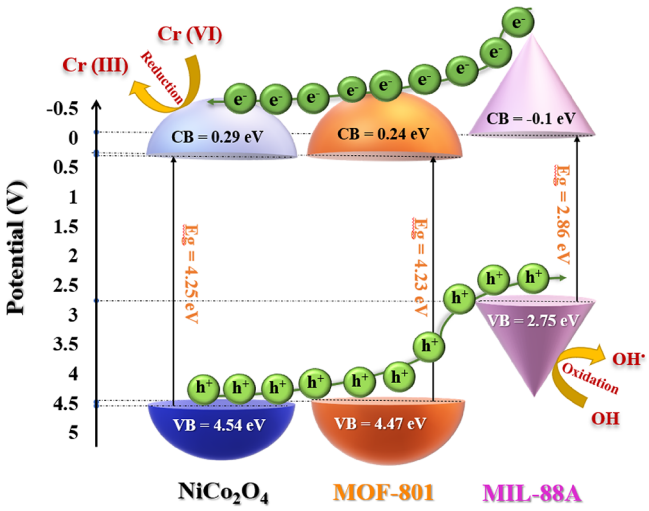

Figure 10. Possible electron transfer mechanism over the $NiCo_2O_4$@MOF-801@MIL-88A composite for chromium reduction.

https://doi.org/10.1021/acsomega.2c05000
ACS Omega 2022, 7, 42901−42915

On the other hand, the Fe(III)-O clusters on the surface of $NiCo_2O_4$@MOF-801@MIL-88A can catalyze the decomposition of H_2O_2 to produce $^{\bullet}OH$ radicals. The $^{\bullet}OH$ radicals yielded by the photo-Fenton reaction contributed to eliminating organic pollutants such as meropenem.

Advanced oxidation processes (AOPs) have been proposed as replaceable solutions for degrading persistent organic compounds because the hydroxyl radicals (·OH) unselectively promote organic substance oxidation at high reaction rates. In short, the combination of Fe^{2+} and H_2O_2 is called a conventional Fenton reaction, which belongs to a type of classical AOP. As the merits of Fenton progress, it is normally operated under ambient temperature and pressure and generate strongly oxidizing radical species (primarily ·OH) for the complete decomposition of organic pollutants into nontoxic products, such as CO_2, H_2O, and inorganic salts.

Besides the Fenton process, photocatalytic oxidation has also been considered an alternative and efficient AOP. The photo-Fenton-like catalytic process is based on the traditional Fenton process and light irradiation. During the Fenton reaction process, the introduction of additional light irradiation leads to the production of more $^{\bullet}OH$ radicals, which benefits from the synergistic effect between the photocatalysis and Fenton reactions. In this project, the photocatalytic activity of the ternary heterojunction was proven through a chromium reaction. In the drug solution, due to the presence of Fe^{2+} and H_2O_2, the photocatalytic and photo-Fenton mechanisms are possible. Based on this background information, many researchers have coupled the Fenton reaction with photocatalysis as a novel technique to treat wastewater. By this means, it is able to realize a win-win situation.

Combining the electrochemical analysis and the photocatalytic experiments, we proposed a possible photocatalytic mechanism of the $NiCo_2O_4$@MOF-801@MIL-88A composite for chromium reduction and meropenem degradation. It can be deduced from the results that the design and synthesis of ternary MOF-based heterojunctions as a photocatalyst were suitable for wastewater treatment.

It is well known that the band energy structures are essential for the in-depth understanding of the interfacial transportation of the photo-induced charge carriers. The coupling of MIL-88A and $NiCo_2O_4$@MOF-801 can enhance the interfacial charge transfer efficiency and reduce the recombination rate of electrons and holes, which are conducive to improved removal efficiency. As a result, the bare MOF-801 and $NiCo_2O_4$ have large bandgaps, but after the construction of the $NiCo_2O_4$@MOF-801@MIL88A heterojunction, the bandgap reduces to 2.55 eV, which is active in the visible light region and can produce electron/hole pairs in the ternary composite.

4. CONCLUSIONS

In summary, a novel double-shelled $NiCo_2O_4$@MOF-801@MIL88A ternary heterojunction was synthesized via a cost-efficient, simple, and safe process. This study has demonstrated that effective photocatalytic reactions eliminate organic and inorganic pollutants. The composite exhibited a higher performance of Cr(IV) reduction and antibiotics degradation (i.e., Meropenem) than the pure components or even the $NiCo_2O_4$@MOF-801 composite under visible light illumination. Furthermore, the effects of drug concentrations, reaction pH, photocatalyst amount, scavenger type, and others have been investigated to achieve the optimized reactions and best response. While the new $NiCo_2O_4$@MOF-801 complex had a good performance in absorbing visible light and removing contaminants, the addition of MIL-88A and changing the bandgap improved the photocatalytic reactions with performances in shorter time. Interestingly, the main photocatalyst, $NiCo_2O_4$@MOF-801@MIL88A, can reduce 100% of Cr(IV) in 45 min, which means that the photocatalytic activity is increased manifold during interface connection and charge carrier separation. Overall, for the first time, our work sheds light on the fabrication of a structure consisting of Ni-cobaltite and MOF for photocatalytic purposes and reports its results in optimal reactions for chromium reduction and meropenem degradation.

■ ASSOCIATED CONTENT

Supporting Information

The Supporting Information is available free of charge at https://pubs.acs.org/doi/10.1021/acsomega.2c05000.

(Figures S1−S3) Powder XRD patterns of $NiCo_2O_4$, MOF-801, and MIL-88A; (Figure S4) FE-SEM images of MOF-801; (Figure S5) elemental mapping and EDX spectrum of $NiCo_2O_4$@MOF-801; (Figure S6) kinetics plots during photoreaction over various photocatalysts (initial [Cr(VI)] = 10 mg/L); (Figure S7) leaching plot of the $NiCo_2O_4$@MOF-801@MIL88A photocatalyst for chromium reduction; (Figure S8) photocatalytic efficiency by $NiCo_2O_4$@MOF-801@MIL88A for photodegradation of antibiotics after 60 min; and (Figure S9) kinetics plots during photodegradation of chromium over various photocatalysts (PDF)

■ AUTHOR INFORMATION

Corresponding Author

Vahid Safarifard − *Department of Chemistry, Iran University of Science and Technology, Tehran 16846-13114, Iran;* orcid.org/0000-0003-4876-8257; Email: vsafarifard@iust.ac.ir

Authors

Mahnaz Bakhtian − *Department of Chemistry, Iran University of Science and Technology, Tehran 16846-13114, Iran*

Negin Khosroshahi − *Department of Chemistry, Iran University of Science and Technology, Tehran 16846-13114, Iran*

Complete contact information is available at: https://pubs.acs.org/10.1021/acsomega.2c05000

Notes

The authors declare no competing financial interest.

■ ACKNOWLEDGMENTS

Support for this investigation by the Iran University of Science and Technology is gratefully acknowledged.

■ REFERENCES

(1) Bahnemann, D. Photocatalytic water treatment: solar energy applications. *Solar energy* **2004**, *77*, 445−459.

(2) Raizada, P.; Soni, V.; Kumar, A.; Singh, P.; Khan, A. A. P.; Asiri, A. M.; Thakur, V. K.; Nguyen, V.-H. Surface defect engineering of metal oxides photocatalyst for energy application and water treatment. *J. Materiomics* **2021**, *7*, 388−418.

(3) Li, S.; Wang, C.; Cai, M.; Yang, F.; Liu, Y.; Chen, J.; Zhang, P.; Li, X.; Chen, X. Facile fabrication of TaON/Bi2MoO6 core−shell S-scheme heterojunction nanofibers for boosting visible-light catalytic

levofloxacin degradation and Cr (VI) reduction. *Chem. Eng. J.* **2022**, *428*, No. 131158.
(4) Tripathy, S. P.; Subudhi, S.; Das, S.; Ghosh, M. K.; Das, M.; Acharya, R.; Acharya, R.; Parida, K. Hydrolytically stable citrate capped Fe3O4@ UiO-66-NH2 MOF: A hetero-structure composite with enhanced activity towards Cr (VI) adsorption and photocatalytic H2 evolution. *J. Colloid Interface Sci.* **2022**, *606*, 353−366.
(5) Goudarzi, M. D.; Khosroshahi, N.; Miri, P.; Safarifard, V., Covalent Organic Frameworks-Based Nanomaterials for Oxygen Evolution Reactions. In *Covalent Organic Frameworks*, CRC Press: pp. 171−184.
(6) Pattappan, D.; Kavya, K.; Vargheese, S.; Kumar, R. T. R.; Haldorai, Y. Graphitic carbon nitride/NH2-MIL-101 (Fe) composite for environmental remediation: Visible-light-assisted photocatalytic degradation of acetaminophen and reduction of hexavalent chromium. *Chemosphere* **2022**, *286*, No. 131875.
(7) Abuzalat, O.; Tantawy, H.; Mokhtar, M.; Baraka, A. Nanoporous bimetallic organic frameworks (Fe/Co)-BDC, a breathing MOF for rapid and capacitive removal of Cr-oxyanions from water. *Journal of Water Process Engineering* **2022**, *46*, No. 102537.
(8) Xu, G.; Du, M.; Zhang, J.; Li, T.; Guan, Y.; Guo, C. Facile fabrication of magnetically recyclable Fe3O4/BiVO4/CuS heterojunction photocatalyst for boosting simultaneous Cr (VI) reduction and methylene blue degradation under visible light. *J. Alloys Compd.* **2022**, *895*, No. 162631.
(9) Koutavarapu, R.; Reddy, C. V.; Syed, K.; Reddy, K. R.; Saleh, T. A.; Lee, D.-Y.; Shim, J.; Aminabhavi, T. M. Novel Z-scheme binary zinc tungsten oxide/nickel ferrite nanohybrids for photocatalytic reduction of chromium (Cr (VI)), photoelectrochemical water splitting and degradation of toxic organic pollutants. *J. Hazard. Mater.* **2022**, *423*, No. 127044.
(10) Habibi-Yangjeh, A.; Asadzadeh-Khaneghah, S.; Feizpoor, S.; Rouhi, A. Review on heterogeneous photocatalytic disinfection of waterborne, airborne, and foodborne viruses: can we win against pathogenic viruses? *J. Colloid Interface Sci.* **2020**, *580*, 503−514.
(11) Akhundi, A.; Habibi-Yangjeh, A.; Abitorabi, M.; Rahim Pouran, S. Review on photocatalytic conversion of carbon dioxide to value-added compounds and renewable fuels by graphitic carbon nitride-based photocatalysts. *Catalysis Reviews* **2019**, *61*, 595−628.
(12) Cheng, T.; Gao, H.; Liu, G.; Pu, Z.; Wang, S.; Yi, Z.; Wu, X.; Yang, H. Preparation of core-shell heterojunction photocatalysts by coating CdS nanoparticles onto Bi4Ti3O12 hierarchical microspheres and their photocatalytic removal of organic pollutants and Cr (VI) ions. *Colloids Surf., A* **2022**, *633*, No. 127918.
(13) Khosroshahi, N.; Goudarzi, M. D.; Safarifard, V. Fabrication of a novel heteroepitaxial structure from an MOF-on-MOF architecture as a photocatalyst for highly efficient Cr (vi) reduction. *New J. Chem.* **2022**, *46*, 3106−3115.
(14) Dai, D.; Qiu, J.; Zhang, L.; Ma, H.; Yao, J. Amino-functionalized Ti-metal-organic framework decorated BiOI sphere for simultaneous elimination of Cr (VI) and tetracycline. *J. Colloid Interface Sci.* **2022**, *607*, 933−941.
(15) Sun, Q.; Han, B.; Li, K.; Yu, L.; Dong, L. The synergetic degradation of organic pollutants and removal of Cr (VI) in a multifunctional dual-chamber photocatalytic fuel cell with Ag@ Fe2O3 cathode. *Sep. Purif. Technol.* **2022**, *281*, No. 119966.
(16) Asadzadeh-Khaneghah, S.; Habibi-Yangjeh, A. g-C3N4/carbon dot-based nanocomposites serve as efficacious photocatalysts for environmental purification and energy generation: a review. *J. Cleaner Prod.* **2020**, *276*, No. 124319.
(17) Moosavi, S. M.; Nandy, A.; Jablonka, K. M.; Ongari, D.; Janet, J. P.; Boyd, P. G.; Lee, Y.; Smit, B.; Kulik, H. J. Understanding the diversity of the metal-organic framework ecosystem. *Nat. Commun.* **2020**, *11*, 1−10.
(18) Khosroshahi, N.; Karimi, M.; Taghvaei, T.; Safarifard, V. Ultrasound-assisted synthesis of CoFe2O4/Ce-UiO-66 nanocomposite for photocatalytic aerobic oxidation of aliphatic alcohols. *Mater. Today Chem.* **2021**, *22*, No. 100582.
(19) Xu, P. P.; Zhang, L.; Jia, X.; Wen, H.; Wang, X.; Yang, S.; Hui, J. A novel heterogeneous catalyst NH 2-MIL-88/PMo 10 V 2 for the photocatalytic activity enhancement of benzene hydroxylation. *Catal. Sci. Technol.* **2021**, *11*, 6507−6515.
(20) Tanhaei, M.; Mahjoub, A. R.; Safarifard, V. Energy-efficient sonochemical approach for the preparation of nanohybrid composites from graphene oxide and metal-organic framework. *Inorg. Chem. Commun.* **2019**, *102*, 185−191.
(21) Zhu, X.-H.; Yang, C.-X.; Yan, X.-P. Metal-organic framework-801 for efficient removal of fluoride from water. *Microporous Mesoporous Mater.* **2018**, *259*, 163−170.
(22) Viswanathan, V. P.; Mathew, S. V.; Dubal, D. P.; Adarsh, N. N.; Mathew, S. Exploring the Effect of Morphologies of Fe (III) Metal-Organic Framework MIL-88A (Fe) on the Photocatalytic Degradation of Rhodamine B. *ChemistrySelect* **2020**, *5*, 7534−7542.
(23) Wang, J.; Wan, J.; Ma, Y.; Wang, Y.; Pu, M.; Guan, Z. Metal−organic frameworks MIL-88A with suitable synthesis conditions and optimal dosage for effective catalytic degradation of Orange G through persulfate activation. *RSC Adv.* **2016**, *6*, 112502−112511.
(24) Li, Y.; Karimi, M.; Gong, Y.-N.; Dai, N.; Safarifard, V.; Jiang, H.-L. Integration of metal-organic frameworks and covalent organic frameworks: Design, synthesis, and applications. *Matter* **2021**, *4*, 2230−2265.
(25) Shao, L.; Yu, Z.; Li, X.; Li, X.; Zeng, H.; Feng, X. Carbon nanodots anchored onto the metal-organic framework NH2-MIL-88B (Fe) as a novel visible light-driven photocatalyst: Photocatalytic performance and mechanism investigation. *Appl. Surf. Sci.* **2020**, *505*, No. 144616.
(26) Chen, D.-D.; Yi, X.-H.; Zhao, C.; Fu, H.; Wang, P.; Wang, C.-C. Polyaniline modified MIL-100 (Fe) for enhanced photocatalytic Cr (VI) reduction and tetracycline degradation under white light. *Chemosphere* **2020**, *245*, No. 125659.
(27) Dao, X.-Y.; Xie, X.-F.; Guo, J.-H.; Zhang, X.-Y.; Kang, Y.-S.; Sun, W.-Y. Boosting photocatalytic CO2 reduction efficiency by heterostructures of NH2-MIL-101 (Fe)/g-C3N4. *ACS Appl. Energy Mater.* **2020**, *3*, 3946−3954.
(28) Fu, H.; Song, X.-X.; Wu, L.; Zhao, C.; Wang, P.; Wang, C.-C. Room-temperature preparation of MIL-88A as a heterogeneous photo-Fenton catalyst for degradation of rhodamine B and bisphenol a under visible light. *Mater. Res. Bull.* **2020**, *125*, No. 110806.
(29) Amaro-Gahete, J.; Klee, R.; Esquivel, D.; Ruiz, J. R.; Jimenez-Sanchidrian, C.; Romero-Salguero, F. J. Fast ultrasound-assisted synthesis of highly crystalline MIL-88A particles and their application as ethylene adsorbents. *Ultrason. Sonochem.* **2019**, *50*, 59−66.
(30) Liu, C.; Wang, J.; Wan, J.; Yu, C. MOF-on-MOF hybrids: Synthesis and applications. *Coord. Chem. Rev.* **2021**, *432*, No. 213743.
(31) Chameh, B.; Khosroshahi, N.; Bakhtian, M.; Moradi, M.; Safarifard, V. MOF derived CeO2/CoFe2O4 wrapped by pure and oxidized g-C3N4 sheet as efficient supercapacitor electrode and oxygen reduction reaction electrocatalyst materials. *Ceram. Int.* **2022**, 22254.
(32) Chang, W.; Xue, W.; Liu, E.; Fan, J.; Zhao, B. Highly efficient H2 production over NiCo2O4 decorated g-C3N4 by photocatalytic water reduction. *Chem. Eng. J.* **2019**, *362*, 392−401.
(33) Liu, J.; Lin, C.; Yao, H.; Zhang, S.; Fang, D.; Jiang, L.; Wang, D.; Zhang, Z.; Wang, J. Construction of high-proportion ternary dual Z-scheme Co3O4/NiCo2O4/NiO photocatalytic system via incomplete solid phase chemical reactions of Co (OH) 2 and Ni (OH) 2 for organic pollutant degradation with simultaneous hydrogen production. *J. Power Sources* **2021**, *506*, No. 230159.
(34) Jayachandran, M.; Maiyalagan, T.; Vijayakumar, T.; Gunasekaran, B. Metal-organic framework (MOF-5) incorporated on NiCo2O4 as electrode material for supercapacitor application. *Mater. Lett.* **2021**, *302*, 130338.
(35) Gonçalves, J. M.; Rocha, D. P.; Silva, M. N.; Martins, P. R.; Nossol, E.; Angnes, L.; Rout, C. S.; Munoz, R. A. Feasible strategies to promote the sensing performances of spinel MCo 2 O 4 (M= Ni, Fe, Mn, Cu and Zn) based electrochemical sensors: a review. *J. Mater. Chem. C* **2021**, *9*, 7852−7887.

https://doi.org/10.1021/acsomega.2c05000
ACS Omega 2022, 7, 42901−42915

(36) Kumar, R. NiCo2O4 nano−/microstructures as high-performance biosensors: a review. *Nano-Micro Letters* **2020**, *12*, 1−52.
(37) Zhang, C.; Li, J.; Shu, L.; Zhao, Y.; Zhang, Y.; Wen, Y.; Qin, H.Design of rod-like NiCo2O4 with nanostructure derived from ZIF-67 as excellent material for supercapacitors. *Int. J. Electrochem. Sci.***2021**, *16* ().
(38) Valekar, A. H.; Cho, K.-H.; Chitale, S. K.; Hong, D.-Y.; Cha, G.-Y.; Lee, U.-H.; Hwang, D. W.; Serre, C.; Chang, J.-S.; Hwang, Y. K. Catalytic transfer hydrogenation of ethyl levulinate to γ-valerolactone over zirconium-based metal−organic frameworks. *Green Chem.* **2016**, *18*, 4542−4552.
(39) Taddei, M.; McPherson, M. J.; Gougsa, A.; Lam, J.; Sewell, J.; Andreoli, E. An optimised compaction process for zr-fumarate (MOF-801). *Inorganics* **2019**, *7*, 110.
(40) Liao, X.; Wang, F.; Wang, F.; Cai, Y.; Yao, Y.; Teng, B.-T.; Hao, Q.; Shuxiang, L. Synthesis of (100) surface oriented MIL-88A-Fe with rod-like structure and its enhanced fenton-like performance for phenol removal. *Appl. Catal., B* **2019**, *259*, No. 118064.
(41) Yan, X.; Jin, Z.; Zhang, Y.; Liu, H.; Ma, X. Controllable design of double metal oxide (NiCo 2 O 4)-modified CdS for efficient photocatalytic hydrogen production. *Phys. Chem. Chem. Phys.* **2019**, *21*, 4501−4512.
(42) Chen, W.; Zhang, Z.; Hou, L.; Yang, C.; Shen, H.; Yang, K.; Wang, Z. Metal-organic framework MOF-801/PIM-1 mixed-matrix membranes for enhanced CO2/N2 separation performance. *Sep. Purif. Technol.* **2020**, *250*, No. 117198.
(43) Iacomi, P.; Formalik, F.; Marreiros, J.; Shang, J.; Rogacka, J.; Mohmeyer, A.; Behrens, P.; Ameloot, R.; Kuchta, B.; Llewellyn, P. L. Role of structural defects in the adsorption and separation of C3 hydrocarbons in Zr-fumarate-MOF (MOF-801). *Chem. Mater.* **2019**, *31*, 8413−8423.
(44) Khosroshahi, N.; Bakhtian, M.; Safarifard, V. Mechanochemical Synthesis of Ferrite/MOF nanocomposite: Efficient photocatalyst for the removal of Meropenem and hexavalent Chromium from water. *J. Photochem. Photobiol., A* **2022**, No. 114033.
(45) Zhang, J.; Bai, H.-J.; Ren, Q.; Luo, H.-B.; Ren, X.-M.; Tian, Z.-F.; Lu, S. Extra Water- and Acid-Stable MOF-801 with High Proton Conductivity and Its Composite Membrane for Proton-Exchange Membrane. *ACS Appl. Mater. Interfaces* **2018**, *10*, 28656−28663.
(46) Jiang, J.; Wang, X.; Zhang, C.; Li, T.; Lin, Y.; Xie, T.; Dong, S. Porous 0D/3D NiCo2O4/g-C3N4 accelerate emerging pollutant degradation in PMS/vis system: Degradation mechanism, pathway and toxicity assessment. *Chem. Eng. J.* **2020**, *397*, No. 125356.
(47) Wan, Y.; Chen, J.; Zhan, J.; Ma, Y. Facile synthesis of mesoporous NiCo2O4 fibers with enhanced photocatalytic performance for the degradation of methyl red under visible light irradiation. *J. Environ. Chem. Eng.* **2018**, *6*, 6079−6087.
(48) Wang, L.; Zhang, Y.; Li, X.; Xie, Y.; He, J.; Yu, J.; Song, Y. The MIL-88A-derived Fe3O4-carbon hierarchical nanocomposites for electrochemical sensing. *Sci. Rep.* **2015**, *5*, 1−12.
(49) Viswanathan, V. P.; Divya, K.; Dubal, D. P.; Adarsh, N. N.; Mathew, S. Ag/AgCl@ MIL-88A (Fe) heterojunction ternary composites: towards the photocatalytic degradation of organic pollutants. *Dalton Trans.* **2021**, *50*, 2891−2902.
(50) Khosroshahi, N.; Goudarzi, M. D.; Gilvan, M. E.; Safarifard, V. Collocation of MnFe2O4 and UiO-66-NH2: An efficient and reusable nanocatalyst for achieving high-performance in hexavalent chromium reduction. *J. Mol. Struct.* **2022**, *1263*, No. 132994.
(51) Mu, R.; Xu, Z.; Li, L.; Shao, Y.; Wan, H.; Zheng, S. On the photocatalytic properties of elongated TiO2 nanoparticles for phenol degradation and Cr (VI) reduction. *J. Hazard. Mater.* **2010**, *176*, 495−502.
(52) Zeng, J.; Song, T.; Lv, M.; Wang, T.; Qin, J.; Zeng, H. Plasmonic photocatalyst Au/gC 3 N 4/NiFe 2 O 4 nanocomposites for enhanced visible-light-driven photocatalytic hydrogen evolution. *RSC Adv.* **2016**, *6*, 54964−54975.
(53) Liqiang, J.; Yichun, Q.; Baiqi, W.; Shudan, L.; Baojiang, J.; Libin, Y.; Wei, F.; Honggang, F.; Jiazhong, S. Review of photoluminescence performance of nano-sized semiconductor materials and its relationships with photocatalytic activity. *Sol. Energy Mater. Sol. Cells* **2006**, *90*, 1773−1787.
(54) Zeng, W.; Wang, L.; Shi, H.; Zhang, G.; Zhang, K.; Zhang, H.; Gong, F.; Wang, T.; Duan, H. Metal−organic-framework-derived ZnO@ C@ NiCo 2 O 4 core−shell structures as an advanced electrode for high-performance supercapacitors. *J. Mater. Chem. A* **2016**, *4*, 8233−8241.
(55) Zhang, D.; Liang, S.; Yao, S.; Li, H.; Liu, J.; Geng, Y.; Pu, X. Highly efficient visible/NIR photocatalytic activity and mechanism of Yb3+/Er3+ co-doped Bi4O5I2 up-conversion photocatalyst. *Sep. Purif. Technol.* **2020**, *248*, No. 117040.

https://doi.org/10.1021/acsomega.2c05000
ACS Omega 2022, 7, 42901−42915